Small-scale convection in the upper mantle beneath the Chinese Tian Shan Mountains

Jie Liu [a,*], Qi-Yuan Liu [a], Biao Guo [a], David A. Yuen [b], Hui-Zhen Song [a]

[a] *State Key Laboratory of Earthquake Dynamics, Institute of Geology,*
China Earthquake Administration, Beijing 100029, China
[b] *Department of Geology and Geophysics & Minnesota Supercomputer Institute,*
University of Minnesota, Minneapolis, MN 55455-0219, USA

Abstract

Small-scale convection of the upper mantle beneath the Chinese Tian Shan (Tien Shan) is investigated in terms of numerical modeling. The finite element method combined with the marker-in-cell technique is used to describe the flow of the heterogeneous upper mantle. The density model is derived from the P-wave velocity structure of the crust and upper mantle along the Kuche–Kuitun profile across the Chinese Tian Shan, which is obtained using the seismic travel time tomography technique. Our computational results reveal the southward-counterclockwise and northward-clockwise upper mantle convective cells underneath the Junggar-north Tian Shan and Tarim-south Tian Shan, respectively. Our results also show the convective scale reaches to ∼500 km and the convective speed at the top of the upper mantle should not be less than 20 mm/year for a normal viscosity model. The northward extrusion of the Tarim block plays a key role in the Tian Shan mountain building since the Cenozoic period, but it nearly does not influence the upper mantle convection. The present-day tectonic deformation in the Chinese Tian Shan is related to the small-scale convection of the upper mantle.
© 2007 Elsevier B.V. All rights reserved.

Keywords: Tian Shan; Upper-mantle convection; Mountain building; Finite element method; Marker-in-cell method

1. Introduction

The Tian Shan range is the largest and present-day most active intracontinental orogenic belt in the world (Fig. 1a). The Tian Shan dynamics has a great value for understanding the basic questions of continental dynamics, especially, the intracontinental deformation and its mechanism.

The recent GPS measurements show that the shortening rate across the western Tian Shan (76°E) is ∼20 mm/year and that across the eastern Tian Shan (87°E) is only ∼3.5 mm/year (Abrakhmatov et al., 1996; Wang et al., 2000). This attests to the fact that the crustal shortening rate of the Tian Shan range decreases eastward, although its mechanism is still poorly understood. Especially, it is also unclear how the deformation measured on the surface is related to the deformation within the crust and upper mantle (Vinnik et al., 2002). Usually, the rejuvenation of the Tian Shan since Miocene is attributed to the collision between the India and Eurasia plate and the effects conveyed though the Tarim block (Molnar and Tapponnier, 1975; England and Houseman,

* Corresponding author. Tel.: +86 10 62009009;
fax: +86 10 62009009.
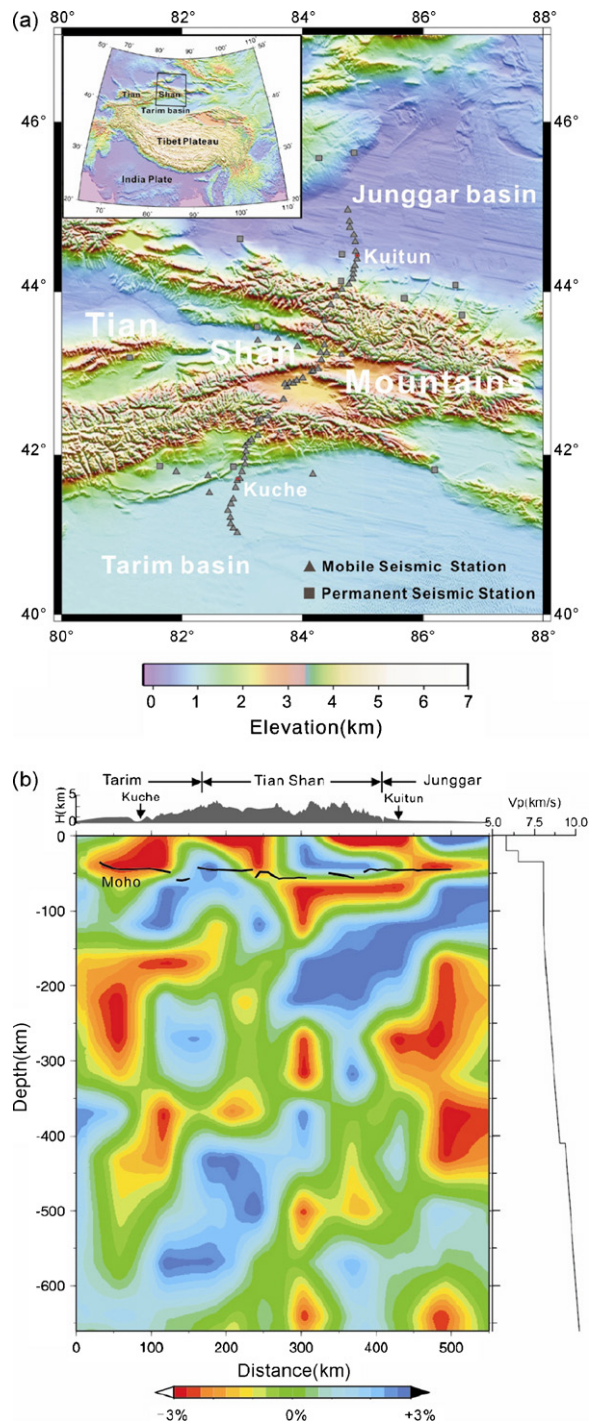*E-mail address:* liujieigcea@gmail.com (J. Liu).

Fig. 1. The seismic station map across the Chinese Tian Shan (a) and the P-wave velocity perturbation in the crust and upper mantle along the Kuche–Kuitun profile (b). The topography of the Tian Shan and adjacent area is shown in the top-left of (a) and the frame with black solid line indicates the research area in this study. The black solid line in (b) represents the Moho discontinuity, which is taken from that by Li et al. (2007). The IASP91 P-wave velocity model is shown in the right side of (b).

1986; Deng et al., 2000). However, the influence of the upper mantle and its relationship with the extrusion of the Tarim block remains uncertain for the Tian Shan orogenics.

Analysis of teleseismic residuals by Vinnik and Saipekova (1984) show the low-velocity anomalies in the upper mantle beneath the central Tian Shan. Based on seismic tomographic images of the crust and upper mantle underneath the western and central Tian Shan, Roecker et al. (1993) proposed a hot and weak upper mantle beneath the mountain range, suggesting an alternative explanation for the rejuvenation of the Tian Shan. Based on the SKS splitting data, Makeyeva et al. (1992) proposed a hot upwelling upper mantle beneath the central Tian Shan related to the small-scale convection. Wolfe and Vemon (1998) analyzed the SKS splitting data across the north central Tian Shan recorded by the Kyrgyzstan seismic network (KNET) and found a pattern of short-wavelength anisotropic heterogeneity, suggesting the complex mantle flow related to the small-scale convection. They also proposed that the mantle flow is not directly coupled with the crust deformation in the Tian Shan range.

By analyzing the gravity data, Fu et al. (1998) proposed the possibility of the small-scale upper mantle convection underneath the Chinese Tian Shan. Their results show a complex convective pattern beneath the mountain range and adjacent area. Poupinet et al. (2002) presented the P-wave velocity structure of the lithosphere along the Kuche–Kuitun profile across the Chinese Tian Shan from the movable seismic array observations, suggesting a high-velocity upper mantle and intracontinental subduction along the profile. This implies that the small-scale convection is centralized in the middle of the profile. Up to now, however, the deformation and movement of the upper mantle beneath the Chinese Tian Shan is still unclear.

Our objective in this study is to investigate whether there is the small-scale convection of the upper mantle beneath the Chinese Tian Shan. For this purpose, the finite element method combined with the marker-in-cell technique is used. Our results would be helpful for understanding the problems mentioned above.

2. The crust and upper mantle velocity structure beneath the Chinese Tian Shan

Our first object is to understand the crust and upper mantle velocity structure beneath the Chinese Tian Shan. Other than the work by Poupinet et al. (2002), several results, especially along the Kuche–Kuitun profile, were presented inside of China, including the deep seismic

sounding and 3D seismic tomography (Xu et al., 2000; Zhao et al., 2003; Xiao et al., 2004). However, these results just offered the structure down to the depth of 300 km or presented the structure of the upper mantle with horizontal resolution larger than 165 km, which is not satisfied for solving our problem and a higher resolution image of the crust and upper mantle velocity structure will be required for investigating the deformation and movement of the upper mantle by numerical modeling.

From April 2003 to September 2004, State Key Laboratory of Earthquake Dynamics, Institute of Geology, China Earthquake Administration, deployed a passive seismic array consisting of 60 broadband stations (Fig. 1a). It can be seen from Fig. 1a that this array is composed of three profiles. One of them is the profile of ~500 km long from Kuche to Kuitun across the Chinese Tian Shan. Li et al. (2007) investigated the S-wave velocity structure of the crust and upper mantle down to 100 km along this profile by using the non-linear receiver function inversion technique (Liu et al., 1996). Their results show that the crust beneath the Chinese Tian Shan has a laterally blocked structure and the averaged thickness of the crust is ~50 km.

From the travel time data of the P-arrivals recorded by this movable seismic array and permanent stations of the Xinjiang regional seismic network, Guo et al. (2006) presented the P-wave perturbation image of the crust and upper mantle down to the depth of 400 km along the Kuche–Kuitun profile by using the travel time tomographic technique (Zhao et al., 1992, 1994). The lateral resolution of their results reaches to 55 km. However, the velocity model of the upper mantle down to the depth of 660 km will be expected to simulate the deformation and movement of the upper mantle. For this purpose, it is reconstructed in this study using the same data and same technique. To reserve the original resolution, the velocity structure from the ground surface to the depth of 400 km is fixed in our reconstruction procedure.

Fig. 1b shows the P-wave velocity perturbation of the crust and upper mantle along the Kuche–Kuitun profile and the Moho boundary given by the receiver function study (Li et al., 2007). Fig. 1b also shows the background P-wave velocity, which is taken from the IASP91 model (Kennett and Engdahl, 1991). It should be noted that the P-wave velocity in the IASP91 model is increased with depth. It can be seen from Fig. 1b that underneath the Tarim and Junggar basin exist obvious low-velocity anomalies in the depth of 150–450 km and a clear high-velocity anomaly in the depth of 60–250 km, which thrusts with a dip angle of ~30° southward from

the Junggar basin and extends intermittently to the depth of ~600 km. The maximal P-wave velocity perturbation reaches to 6% in the upper mantle along this profile, which implies that large density or temperature anomalies exist in the upper mantle beneath the Chinese Tian Shan. This encourages us to study the possibility of the small-scale convection driven by the density anomalies beneath the Chinese Tian Shan.

3. Method

Since 1980s, the finite element method (FEM) has become one of important tools of investigating the mantle convection (Christensen, 1984; King et al., 1990; Moresi and Gurnis, 1996; Zhong et al., 2000). Usually, the creeping flow problem is solved with the Eulerian description. Due to the mesh grids are fixed in the Eulerian description, the position of material at the current nodal point will be difficult to be determined in the next moment. Thus, the Eulerian description is hard to be used for determining the time-dependent shape variations in heterogeneous media.

The so-called marker-in-cell (MIC) or particle-in-cell (PIC) algorithm for the Eulerian method was proposed firstly by Harlow and Welch (1965). Their main idea is that the micro-elements called the markers or particles are filled in cells to mark the material property. In terms of the marker's movement, the material deformation is described easily. These have been used in solving the geodynamic problems (Weinberg and Schmeling, 1992; Schott and Schmeling, 1998). The numeric technique used could be the FEM or the finite difference method (Gerya and Yuen, 2003; Moresi et al., 2003; Tackley and King, 2003).

A new technique of combining the FEM with the MIC algorithm was proposed by Liu et al. (2006), which has been verified with benchmarks (Travis et al., 1990). In terms of the modularized design, their computation program is easily extensible and will be used in this study. The main idea of this method is given in Appendix A.

4. Model and boundary conditions

In this section, we shall discuss the earth model used for our numerical simulation. In principle, the numerical simulation of the mantle convection should be a 3D problem. However, due to lack of high-resolution 3D seismic tomographic data, our work has to be limited to the 2D case.

Our P-wave velocity model of the crust and upper mantle along the Kuche–Kuitun profile is derived from

the P-wave velocity perturbation and the IASP91 model shown in Fig. 1b. The crustal thickness of our model is 50 km. Then, the density distribution in the crust and upper mantle can be estimated further from the P-wave velocity model in terms of the Birch's law (Birch, 1960, 1961):

$$\rho_c = 0.2676V_p + 1.1733,$$
$$\rho_m = 0.3413V_p + 0.5588 \tag{1}$$

where V_p denotes P-wave velocity, ρ_c and ρ_m denote the density of the crust and upper mantle, respectively. The coefficients in the Eq. (1) can be obtained from the IASP91 model (Kennett and Engdahl, 1991). It should be noted that the density is increased with depth in our crust and upper mantle model.

However, as mentioned above, the length of our profile is only 550 km long. Our numerical tests demonstrate that such a size is not enough, so that the obvious boundary effects will appear in the upper mantle convective simulation. Thus, we have to enlarge the horizontal size of our density model to avoid this problem. For this purpose, the density contours on both sides are stretched horizontally.

Our density model used in this study is shown in Fig. 2, from which we can see that the size of our density model reaches to 990 km in the horizontal direction and the aspect ratio reaches to 1:1.5. The thick line in Fig. 2 indicates the bottom boundary of the lithosphere determined according to the density contour of 3.4 g/cm³. It should be pointed out that this is a result after smoothing in order to restrain its undulations. It can be seen from Fig. 2 that the lithospheric thickness in our model is ~140 km beneath the mountain range and it reaches

to ~240 and ~250 km beneath the Tarim and Junggar block, respectively. It is known that the lithospheric thickness at the continental root is about 150–250 km (Schubert et al., 2001). According to the observations of the S-wave receiver functions, Kumar et al. (2005) inferred that the lithospheric thickness is 90–120 km beneath the western Tian Shan and 160–270 km underneath the Tarim block. Thus, our result looks reasonable. In addition, Fig. 2 also shows obvious lateral variations of the density underneath the Tian Shan, which are consistent with the large P-wave velocity perturbations in the same region shown in Fig. 1b.

Usually, in the mantle convection studies, the density model is derived from the temperature and the equation of state (EOS). As mentioned above, however, our density model is derived from the P-wave velocity model given by seismic tomography. Thus, our initial temperature distribution can be derived from a normal temperature model in the crust and upper mantle (Jeanloz and Morris, 1986; Schubert et al., 2001; Stuwe, 2002). In particular, we assume that the temperature of 1200 °C at the lithospheric bottom and a temperature difference of 1700 °C between the ground surface and bottom of the upper mantle. Then, in terms of the linear interpolation, the temperature distribution in the crust and upper mantle can be estimated further. As shown in Fig. 3a, we can see the temperature distribution increased with depth in the upper mantle.

In general, it is uneasy to have an accurate estimation of the mantle viscosity. Usually, the mantle viscosity of 10^{19} to 10^{22} Pa s has been recognized and its lower limitation corresponds to the value for the asthenosphere (King, 1995). The viscosity of 10^{21} Pa s proposed firstly by Haskell (1935, 1936) also has been accepted widely and called the characteristic viscosity of the mantle. The averaged viscosity over the whole mantle is 3×10^{21} Pa s (Karato, 2003). Recently, however, some of new results show that the viscosity of the upper mantle is 10^{20} to 10^{21} Pa s and its averaged value is 4×10^{20} Pa s (Forte and Mitrovica, 2001; Mitrovica and Forte, 2004). Thus, the viscosity of 10^{19} to 10^{21} Pa s could be taken as an accepted estimation for the upper mantle and its upper limitation can reach to 3×10^{21} Pa s. The results mentioned above can be taken as our constraints of the viscosity model in this study.

It is well known that the viscosity depends on several factors, including temperature, pressure and stress, etc. Among these, the temperature and pressure are more important than others (Turcotte and Schubert, 1982). Thus, in our case, we only consider the temperature and pressure. Following Christensen (1984), the dimensionless viscosity of the crust and upper mantle can be
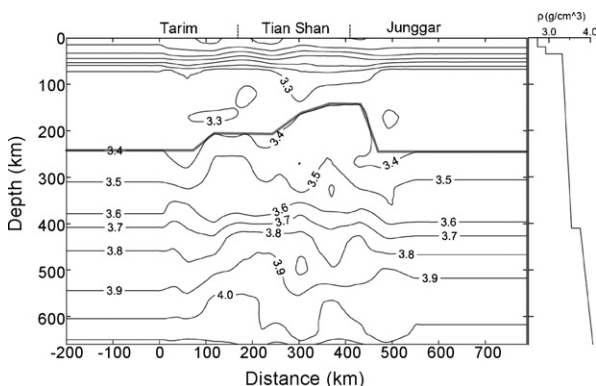

Fig. 2. Density model of the crust and upper mantle beneath the Chinese Tian Shan along the Kuche–Kuitun profile. The digit denotes the density, which unit is g/cm³. The thick line denotes the lithospheric boundary and the fine line denotes the density contour.
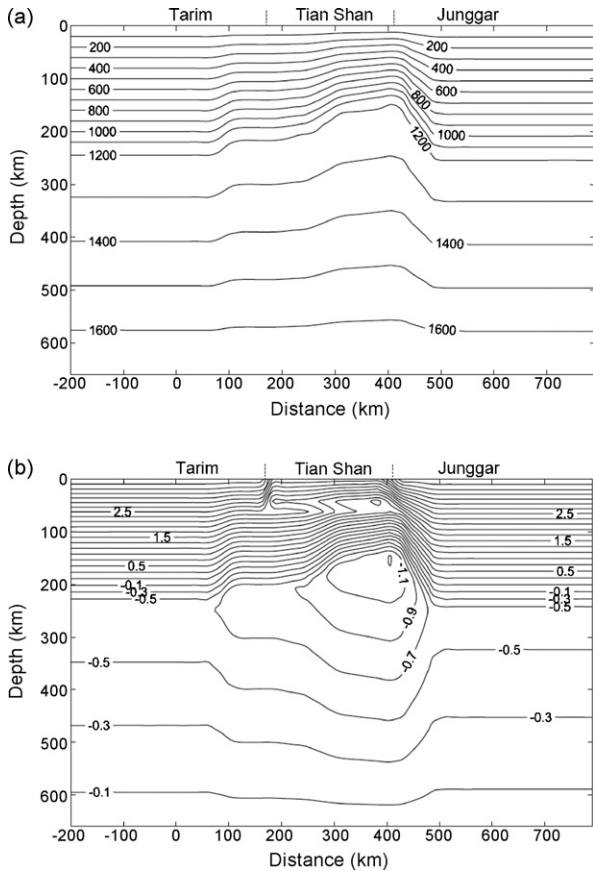
Fig. 3. Temperature and viscosity distribution of the crust and upper mantle along Kuche–Kuitun profile: (a) temperature distribution (°C); (b) viscosity distribution (dimensionless logarithmic value).

estimated using the formula:

$$\eta = \frac{1}{\eta_0} \exp\left[\frac{E + W(1 - z)}{2.088 + T}\right] \tag{2}$$

where η_0 is the reference viscosity; E and W denote the dimensionless activation-energy and activation-volume, respectively; T denotes the dimensionless temperature; z is the dimensionless scale in the vertical direction, which is zero at the bottom and equals 1 at the top of our model. It can be seen from Eq. (2) that the viscosity is decreased, when the temperature is increased, and increased with depth or pressure.

In this study, the parameters of E and W are taken from those given by Christensen (1984). The former studies show that the viscosity near the ground surface is ∼10^{25} Pa s (Schott and Schmeling, 1998; Burov and Guillou-Frottier, 2005). Our computational results by Eq. (2) are close to this value.

The GPS observations demonstrate that the Chinese Tian Shan crust has a shortening rate of 7–8 mm/year

along the Kuche–Kuitun profile (Wang et al., 2000). To simulate this shortening crust, a lateral variation of the crustal viscosity is assumed. For this purpose, the viscosity of the crust beneath the Tian Shan range is assumed to be only 10% of the result given by Eq. (2). This implies that we have a weakened crust beneath the Tian Shan rang and solid basins on both sides. This assumption is mainly based on the GPS data and our numerical tests. Although this assumption is something subjective, it is still reasonable and feasible for our study. This is because that the crust does not involve the mantle convection and the simulation of the crustal deformation is not our main purpose in this study.

Fig. 3b shows our viscosity model of the crust and upper mantle. It should be pointed out that Fig. 3b is merely one of different possible viscosity distributions along the profile, which have been considered also relevant to different lithospheric thickness, temperature distributions as well as the parameters in Eq. (2). Our tests manifest that the result shown in Fig. 3b seems to be more reasonable than others.

On the top of our model, a free boundary is placed, which corresponds to the ground surface, and in the bottom and two side-boundaries are set the free-slip boundary. The temperatures at the top and bottom are fixed in our model. The thermal fluxes on two side-boundaries are assumed to be zero.

5. Results

Fig. 4a and b shows our computational results of the small-scale convection underneath the Chinese Tian Shan based on two different models, unextended and extended model, respectively. In these computations, the boundary conditions without the external force are applied to the model. It can be seen from Fig. 4 that obvious boundary effects appear in Fig. 4a and this phenomenon does not appear in Fig. 4b, from which we can see that the main part of the convection cell is limited merely to the unextended range of the model. Comparing Fig. 4a with Fig. 4b, we find that the convection cells for these two models are quite similar each to other in the unextended range.

In addition, Fig. 4b also illustrates that underneath the Junggar basin and north Tian Shan exists a southward-counterclockwise convection and its convective scale reaches to ∼500 km in both of vertical and horizontal direction. In addition, a weak northward-clockwise convection exists underneath the Tarim basin and south Tian Shan. These two convection cells merged nearby the south border of the mountain range. This implies that due to the drag effects of the mantle convection,
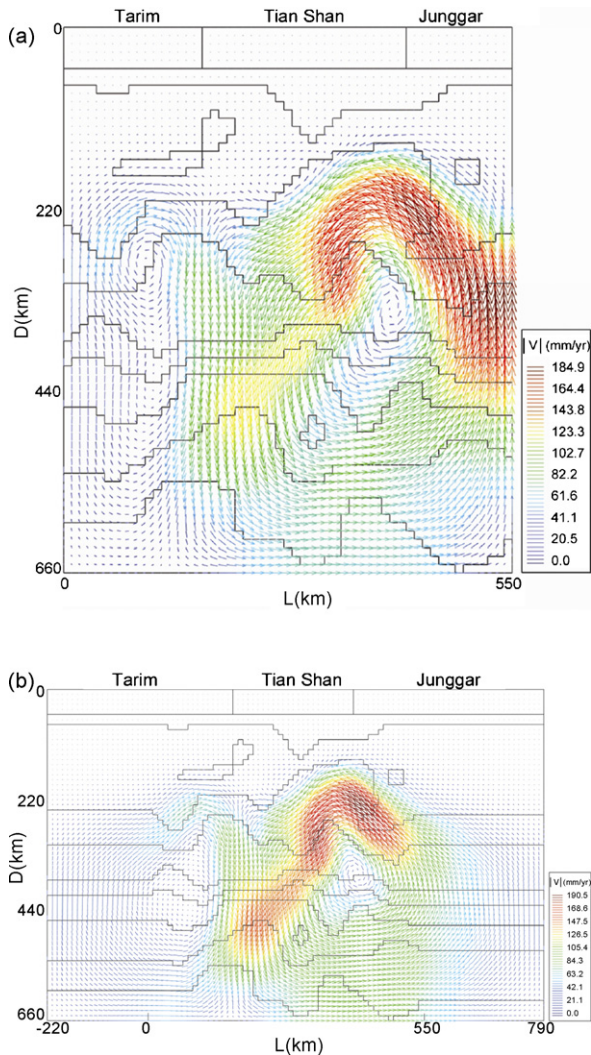
Fig. 4. The upper mantle convection driven by density anomalies: (a) unextended model; (b) extended model. Arrows denote the vectors of convection velocity. The magnitude of velocity is scaled by the length and colour of the arrows. Black lines indicate the density contours in the upper mantle at the initial state and the bounds of mountains and basins in the crust.

the Tarim and Junggar lithosphere are converged and thrust down into the upper mantle beneath the Tian Shan. These observations are consistent with the conjectures proposed from the receiver function study by Li et al. (2007) and seismic tomography study by Guo et al. (2006). The maximal convective velocity in Fig. 4b emerges at the border between the north Tian Shan and Junggar basin. Here we have the maximal density differential and the minimal viscosity along the whole profile.

Since our viscosity model is Newtonian, the speed of the mantle flow is inversely proportional with the viscos-

ity (Fowler, 1985). When all of parameters of our model used are kept same, except the viscosity, our numerical tests demonstrate that the upper mantle convection can have a similar pattern for different viscosity models, although the convective speed can have different magnitude. In particular, when taking a homogeneous viscosity model with the viscosity of 3×10^{21} Pa s for the upper mantle and assuming that the viscosity of the crust is 10^{24} Pa s in the mountain range and 10^{25} Pa s in the basin area, our computational results demonstrate that the convective speed at the top of the upper mantle beneath the Tian Shan can reach to $\sim$20 mm/year. According to these results, we infer that the greatest convective speed in the upper mantle underneath the mountain range should not be less than 20 mm/year for any normal viscosity models.

Fig. 5a shows the horizontal velocity distribution on the ground surface relevant to Fig. 4b and manifests that an opposite movement exists between the Tarim and Junggar block, and the shortening rate of the crust in the mountain range is less than 1 mm/year. This is inconsistent with the GPS data (Wang et al., 2000). The corresponding vertical velocity distribution is shown in Fig. 5b, in which the mountain range has a descending movement consisting with the down-welling of the upper mantle. This is also contradictive with the geodesy and geological observations (Peng, 1993; Deng et al., 2000), which show an apparent contemporary uplift. This illustrates that the uplift of the Tian Shan does not rely merely on the upper mantle convection.

In practice, it has been recognized that the Tarim block plays an important role in the uplift of the Tian Shan
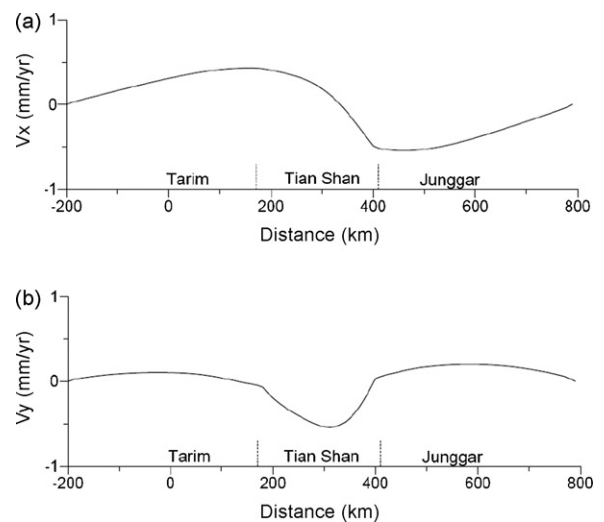

Fig. 5. Velocity distribution on the top boundary of Fig. 4: (a) horizontal velocity distribution; (b) vertical velocity distribution.
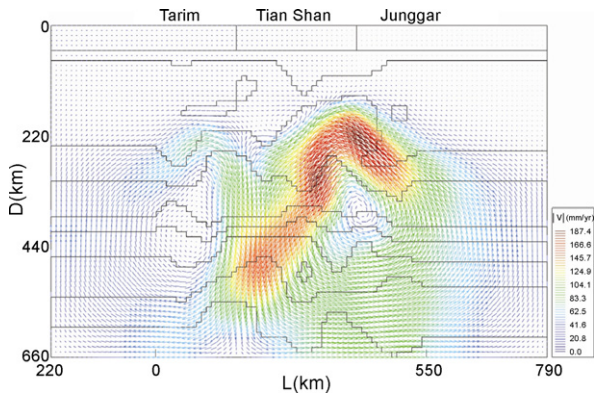
Fig. 6. The upper mantle convection when considering the extrusion of the Tarim (annotations are the same as Fig. 4).

(Avouac et al., 1993; Deng et al., 2000). Therefore, it will be necessary to consider the northward movement of the Tarim in our computation.

According to the GPS data (Wang et al., 2000), we assume that the Tarim crust has a northward movement at the velocity of 7.17 mm/year, which is equal to the dimensionless velocity of 150 in our computation. The result under this boundary condition is shown in Fig. 6, from which we can see that the upper mantle convection is almost no difference from that in Fig. 4b, except that the movement of the Tarim lithosphere becomes slightly faster. This manifests that the northward movement of the Tarim crust nearly does not influence the upper mantle convection. A reason is that the Tarim block is far from the main cell of the upper mantle convection. Another reason is that the movement speed of the Tarim block is much smaller than the mantle flow. When the same boundary condition is extended to the whole lithosphere, our numerical tests demonstrate that the mantle convection is nearly unchanged.

In addition, Fig. 6 also shows that the lower lithosphere of the Junggar block has a component of the southward movement dragged by the convection of the underneath mantle. This could resist the northward movement of the Tarim block. Simultaneously, the lower part of the Tarim lithosphere is impeded and dragged downward by the down-welling of the underneath mantle.

Fig. 7 shows the velocity distribution on the ground surface relevant to Fig. 6. In Fig. 7a is given the comparison of the computational horizontal velocity distribution with the GPS data at 18 stations (Niu et al., 2005), which have been projected on the Kuche–Kuitun profile. Fig. 7a manifests that the simulated deformation of the crust has a tendency similar with the GPS data. This demonstrates our boundary condition is reasonable.
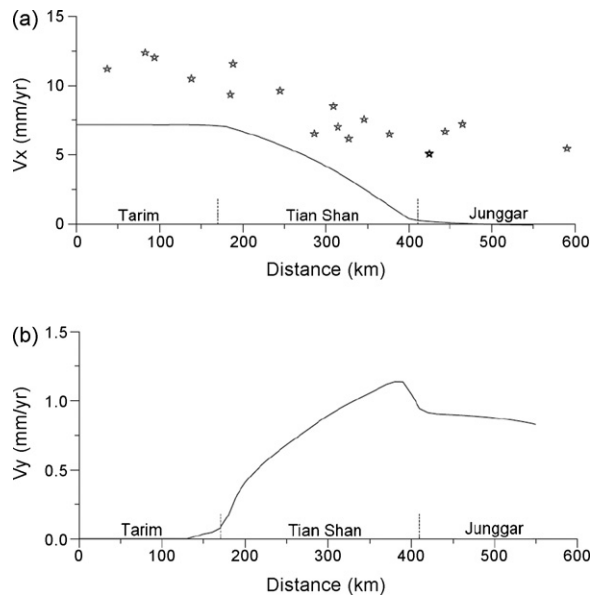

Fig. 7. Velocity distribution on the top boundary of Fig. 6: (a) horizontal velocity distribution and GPS data (denoted by stars); (b) vertical velocity distribution.

Fig. 7b shows the velocity of the simulated vertical movement on the surface, which is completely different from the case shown in Fig. 5b. It can be seen from Fig. 7b that the uplifting rate is increased step by step from the south Tian Shan to north Tian Shan and the maximum rate reaches to ∼1.13 mm/year. This result is consistent with the leveling survey (Peng, 1993). Comparing Fig. 7b with Fig. 5b, we can see that the northward movement of the Tarim block plays the key role in the Cenozoic uplift of the Tian Shan Mountains.

According to the computed principal strain-rate in the mountain range over the depth of 0–120 km (Fig. 8), we found that both of the vertical and horizontal crustal deformation in the north Tian Shan are larger than those in the south Tian Shan. This could be caused by the thin lithosphere underneath the mountain range and the large convective velocity of the underneath upper mantle. Meanwhile, the results shown in Fig. 8 can be used for explaining why the north Tian Shan has a greater uplifting rate than the south Tian Shan (Peng, 1993). This implies that the small-scale upper-mantle convection beneath the Tian Shan not only resists the northward movement of the Tarim block, but also distorts the crust through the heated and thinned lithosphere.

It should be emphasized that all of results shown in Figs. 4–8 just represent the output at the first-time step for a transient problem, which corresponds to the result obtained from the contemporary geophysical data.
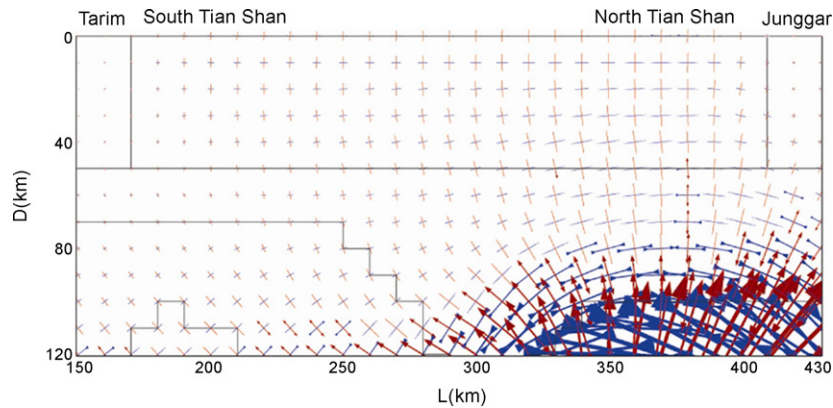
Fig. 8. Principal strain rate of the crust and topmost of upper mantle of the Chinese Tian Shan. Blue arrows denote compressional principal strain rate, red arrows denote tensile's. The length of arrows is proportional to the value of the principal strain rate. (For interpretation of the references to colour in this figure legend, the reader is referred to the web version of the article.)

In this study, we also calculated the evolution of the upper mantle convection, although it is less important. For the convection shown in Fig. 4b, the average kinetic energy will decrease exponentially and remain ∼1% after 1.2 Myears, and the maximal velocity in the profile will be decreased from 190 to 40 mm/year. Simultaneously, the density contour lines will be flattened significantly and the variations of the temperature distribution are similar with those of the density contours. In fact, due to that the northward movement of the Tarim block does not influence the upper mantle convection, the evolution of the convection shown in Fig. 6 is nearly same with that in Fig. 4b.

6. Conclusion and discussion

Based on the tomographic results given by Guo et al. (2006), we reconstruct the seismic tomographic images of the P-wave velocity structure of the crust and upper mantle along the Kuche–Kuitun profile. This new result covers the whole upper mantle beneath the Chinese Tian Shan and makes it possible to build a high-resolution model of the crust and upper mantle, which is used further to simulate the deformation and flow of the upper mantle beneath the Chinese Tian Shan.

In this purpose, the FEM combining with the MIC technique is used. Our results show that the small-scale convection of the upper mantle driven by density anomalies should exist underneath the Chinese Tian Shan. Based on our results, we can have the following conclusions:

(1) The small-scale convections underneath the Chinese Tian Shan are composed of two convective cells: one

is the weak northward-clockwise convection underneath the Tarim and south Tian Shan; the other is the strong southward-counterclockwise convection underneath the Junggar and north Tian Shan, which scale reaches to ∼500 km.

(2) The northward movement of the Tarim block nearly does not influence the upper mantle convection beneath the Chinese Tian Shan and the convective speed at the top of the upper mantle underneath the mountain range should not be less than 20 mm/year for a normal viscosity model of the upper mantle.

(3) The northward extrusion of the Tarim block plays a key role in the Cenozoic orogeny of the Chinese Tian Shan, and the present-day tectonic deformation of the orogeny is related to the upper mantle convection.

It should be point out that our crustal model is relatively simple in our computations. Moreover, our computations are limited to the 2D case. Especially, our discussions deal only with the crust and upper mantle along the Kuche–Kuitun profile, which is almost perpendicular to the mountain strike. In general, in the young orogenic belt, the deformation of the upper mantle should be parallel with the mountain strike (Meissner et al., 2002). Chen et al. (2005) also reported the results about the S-wave splitting from the data recorded by a movable array across the Chinese Tian Shan located at 86°E–88°E, suggesting a fast direction roughly parallel with the mountain strike along their observational profile. Therefore, the 3D small-scale convection beneath the Tian Shan remains still an open question. For this purpose, the 3D velocity structure of the crust and upper mantle will be required.

Appendix A

A.1. Governing equations and solving strategy

The physical process of the upper mantle convection can be described by the conservation equations of mass, momentum and energy (Schubert et al., 2001). We assume that the medium is incompressible and the Prandtl number is infinite. In this study, we adopt the Boussinesq approximation. Thus, the governing equations can be written as

$$\frac{\partial v_i}{\partial x_i} = 0, \tag{A1}$$

$$-\frac{\partial p}{\partial x_i} + \frac{\partial \sigma_{ij}}{\partial x_j} = -\rho g_i \tag{A2}$$

$$\frac{\partial T}{\partial t} + v_i \frac{\partial T}{\partial x_i} - \kappa \frac{\partial^2 T}{\partial x_i^2} = \frac{H}{\rho c} \tag{A3}$$

where v_i and x_i ($i = 1, 2, 3$) are the velocity vector and coordinates, respectively; p is the hydrodynamic pressure; σ_{ij} is the deviatoric stress tensor; ρ is the density related to the composition and temperature; g_i is the ith component of gravitational acceleration; T and t represent the temperature and time, respectively; H is the radioactive heating production in an unit volume; κ is the coefficient of thermal diffusion, $\kappa = k/\rho C$, k is the thermal conductivity, c is the specific heat. The deviatoric stress tensor can be related to the strain rate $\dot{\varepsilon}_{ij}$ in terms of the constitutive equation:

$$\sigma_{ij} = 2\eta \dot{\varepsilon}_{ij} = \eta \left(\frac{\partial v_i}{\partial x_j} + \frac{\partial v_j}{\partial x_i} \right) \tag{A4}$$

where η is the viscosity.

The relationship between the density and temperature can be described by the equation of state (EOS):

$$\rho = \rho_0[1 - \alpha(T - T_0)] \tag{A5}$$

where $\rho_0 = \rho(T_0)$ refers to the reference density, and T_0 is the reference temperature, α is the thermal expansion coefficient.

To preserve the numerical stability, we use the dimensionless variables. The dimensionless form of the conservation equations can be obtained from the scale coefficients:

$$x_i' = \frac{x_i}{D}, \qquad t' = t\frac{\kappa}{D^2}, \qquad v_i' = v_i \frac{D}{\kappa},$$

$$p' = p\frac{D^2}{\eta_0 \kappa}, \qquad \eta' = \frac{\eta}{\eta_0}, \qquad T' = \frac{T - T_0}{\Delta T}$$

where $'$ represents the dimensionless variable, D is the extent of the vertical direction, η_0 is the reference viscosity, $\Delta T = T_1 - T_0$ is the temperature difference between the top and bottom. It should be pointed out that the EOS (A5), as an independent equation, is not included in the governing equations and the density variable is still retained in the momentum equation during the dimensionless process in our method. This makes it possible to solve our problem, when the density distribution is not derived from the temperature and the EOS.

The governing equations are solved by using the FEM, and the medium movement can be described using the MIC technique. After initializing the element and marking mesh, the following operations will be performed at each time step: (1) solving the momentum equation at the known density; (2) solving the energy equation from the velocity distribution; (3) calculating the velocity and temperature of the markers; (4) determining the new position of the markers according to the step of velocity and time; (5) calculating the new nodal parameters of each element from the position and temperature of markers. These five steps will be performed iteratively, until the terminal condition, i.e. a steady state or a specified time, is satisfied.

A.2. Finite element scheme

The Stokes equation (A2) is solved simultaneously with the continuity equation (A1) given by the pressure-stabilizing Petrov–Galerkin (PSPG) method (Hughes et al., 1986), where the interpolations of the velocity and pressure are equal-order and the numerical stability can be preserved. The key point in this method is to perform additional perturbation stabilization for the pressure-term. For this purpose, we use the weight function:

$$\delta v_i + \frac{\alpha^e (h^e)^2}{2\eta} \frac{\partial \delta p}{\partial x_i} \tag{A6}$$

when establishing the finite element equations by using the weighting residual method. Here h^e is the size of the element, α^e is an adjustable constant.

We use the streamline upwind Petrov–Galerkin (SUPG) algorithm (Brooks and Hughes, 1982) to solve the energy equation. The weight function in the SUPG algorithm is

$$\delta T + \frac{\tilde{k}}{||\boldsymbol{v}_i||} \cdot \boldsymbol{v}_i \frac{\partial \delta T}{\partial \boldsymbol{x}_i} \tag{A7}$$

where $\tilde{k}$ is a variable relying on the size of the element, the velocity and the local Peclet number.

Based on the weight functions, we can have the weak-form of the governing equations. The computational codes can be generated automatically with the finite element program generator (FEPG). The discrete energy equation in time domain is solved in terms of the Crank–Nicolson algorithm.

A.3. Marker-in-cell algorithm

Firstly, the velocity and temperature of markers within the element are obtained by interpolating the results of the FEM and the bi-linear interpolation function is used. In particular, for the rectangular elements, the interpolation function is

$$\begin{aligned} B_m = {} & \left(1 - \frac{\Delta x_m}{dx}\right)\left(1 - \frac{\Delta z_m}{dz}\right) B_i \\ & + \frac{\Delta x_m}{dx}\left(1 - \frac{\Delta z_m}{dz}\right) B_j + \frac{\Delta x_m}{dx}\frac{\Delta z_m}{dz} B_k \\ & + \left(1 - \frac{\Delta x_m}{dx}\right)\frac{\Delta z_m}{dz} B_l \end{aligned} \tag{A8}$$

where B_m is the parameter of the mth marker, B_P ($P = i, j, k, l$) is the parameter at four nodes of each element where the marker is located, dx and dz are the scale of the element in the horizontal and vertical direction, respectively, Δx_m and Δz_m represent the distance of mth marker to the left-bottom corner of the ith node in the x and z direction, respectively.

The new position of the markers can be determined according to the moving speed of the markers calculated by using the Runge–Kutta scheme of the forth-order in the space and first-order in time.

The material density of a marker depends on its current temperature. This can be calculated by the EOS. Simultaneously, the material distribution in different position will be varied with the marker shift. Thus, it is necessary to recalculate the corresponding parameters (density, viscosity coefficient, etc.) at the Eulerian nodal points. The parameters at the Pth node are obtained from the weighted average over all markers in surrounding cells (Gerya and Yuen, 2003). This can be made in terms of the formula:

$$B_P = \frac{\Sigma_m B_m w_m(P)}{\Sigma_m w_m(P)} \tag{A9}$$

where $w_m(P)$ is the statistical weight function of the mth marker at the Pth node. For the rectangular elements:

$$w_m(P) = \left(1 - \frac{\Delta x_{mP}}{dx}\right)\left(1 - \frac{\Delta z_{mP}}{dz}\right)\frac{1}{dxdz} \tag{A10}$$

where Δx_{mP} and Δz_{mP} represent the distance of the mth marker to the node P in the x and z direction, respectively.

References

Abrakhmatov, K.Y., Aldazhanov, S.A., Hager, B.H., Hamburger, M.W., Herring, T.A., Kalabaev, K.B., Makarov, V.I., Molnar, P., Panasyuk, S.V., Prilepin, M.T., Reilinger, R.E., Sadybakasov, I.S., Souter, B.J., Trapeznikov, Y.A., Tsurkov, V.Y., Zubovich, A.V., 1996. Relatively recent construction of the Tien Shan inferred from GPS measurements of present day crustal deformation rates. Nature 384, 450–453.

Avouac, J.P., Tapponnier, P., Bai, M., You, H., Wang, G., 1993. Active thrusting and folding along the Northern Tien Shan and late Cenozoic rotation of the Tarim relative to Dzungarian and Kazakhstan. J. Geophys. Res. 98, 6755–6804.

Birch, F., 1960. The velocity of compressional waves in rocks to 10 kilobars. 1. J. Geophys. Res. 65, 1083–1102.

Birch, F., 1961. The velocity of compressional waves in rocks to 10 kilobars. 2. J. Geophys. Res. 66, 2199–2224.

Brooks, A.N., Hughes, T.J.R., 1982. Streamline upwind/Petrov–Galerkin formulations for convection dominated flows with particular emphasis on the incompressible Navier–Stokes equations. Comput. Methods Appl. Mech. Eng. 32, 199–259.

Burov, E., Guillou-Frottier, L., 2005. The plume head-continental lithosphere interaction using a tectonically realistic formulation for the lithosphere. Geophys. J. Int. 161, 469–490.

Chen, Y.P., Wang, L.S., Mi, N., Li, H., Yu, D.Y., Xu, M.J., Liu, S.W., Li, C., Xu, Z., 2005. Shear wave splitting observations in the Chinese Tianshan orogenic belt. Geophys. Res. Lett. 32, L07306, doi:10.1029/2004GL021686.

Christensen, U., 1984. Convection with pressure- and temperature-dependent non-Newtonian rheology. Geophys. J. Roy. Astr. Soc. 77, 343–384.

Deng, Q.D., Feng, X.Y., Zhang, P.Z., Xu, X.W., Yang, X.P., Peng, S.Z., Li, J., 2000. Active Tectonics of the Chinese Tian Shan Mountains. Seismology Press, Beijing (in Chinese with English Abstract).

England, P., Houseman, G., 1986. Finite strain calculation of continental deformation. 2. Comparison with the India–Asia collision zone. J. Geophys. Res. 91 (B3), 3664–3676.

Forte, A.M., Mitrovica, J.X., 2001. Deep-mantle high-viscosity flow and thermochemical structure inferred from seismic and geodynamic data. Nature 410, 1049–1055.

Fowler, A.C., 1985. On the thermal state of the Earth's mantle. J. Geophys. 53, 42–51.

Fu, R.S., Huang, J.H., Xu, Y.M., Chang, X.H., 1998. Study of the mantle dynamics in the region from Qinghai-Xizang plateau to Tiansha Mountain. Chin. J. Geophys. 41, 658–668 (in Chinese with English Abstract).

Gerya, T.V., Yuen, D.A., 2003. Characteristics-based marker-in-cell method with conservative finite-differences schemes for modeling geological flows with strongly variable transport properties. Phys. Earth Planet. Int. 140, 293–318.

Guo, B., Liu, Q.Y., Chen, J.H., Zhao, D.P., Li, S.C., Lai, Y.G., 2006. Seismic tomography of the crust and upper mantle structure underneath the Chinese Tian Shan. Chin. J. Geophys. 49, 1693–1700.

Harlow, F.W., Welch, J.E., 1965. Numerical calculation of time-dependence viscous incompressible flow of fluid with free surface. Phys. Fluid 8, 2182–2189.

Haskell, N.A., 1935. The motion of a viscous fluid under a surface load. I. Physics 6, 265–269.

Haskell, N.A., 1936. The motion of a viscous fluid under a surface load. II. Physics 7, 56–61.

Hughes, T.J.R., Franca, L.P., Balestra, M., 1986. A new finite element formulation for computational fluid dynamoics. V. Circumventing the Babuska–Brezzi condition: a stable Petrov–Galerkin formulation of the Stokes problem accommodating equal-order Interpolations. Comput. Methods Appl. Mech. Eng. 59, 85–99.

Jeanloz, R., Morris, S., 1986. Temperature distribution in the crust and mantle. Ann. Rev. Earth Planet. Sci. 14, 377–415.

Karato, S., 2003. The Dynamic Structure of the Deep Earth: An Interdisciplinary Approach. Princeton University Press, Princeton.

King, S.D., 1995. Models of mantle viscosity. In: Ahrens, T.J. (Ed.), Mineral and Crystallography: A Handbook of Physical Constants. AGU, Washington, pp. 227–235.

King, S.D., Raefsky, A., Hager, B.H., 1990. ConMan: vectorizing a finite element code for incompressible two-dimensional convection in the Earth's mantle. Phys. Earth Planet. Int. 59, 195–207.

Kennett, B.L.N., Engdahl, E.R., 1991. Travel times for global earthquake location and phase identification. Geophys. J. Int. 105, 429–465.

Kumar, P., Yuan, X., Kind, R., Kosarev, G., 2005. The lithosphere–asthenosphere boundary in the Tien Shan-Karakoram region from S receiver functions: evidence for continental subduction. Geophys. Res. Lett. 32, L07305, doi:10.1029/2004GL022291.

Li, Y., Liu, Q.Y., Chen, J.H., Li, S.C., Guo, B., Lai, Y.G., 2007. Shear wave velocity structure of the crust and upper mantle underneath the Tian Shan orogenic belt. Sci. China Ser. D: Earth Sci. 50 (3), 321–330.

Liu, J., Liu, Q.Y., Song, H.Z., 2006. Numerical method of modeling thermal creeping flow in heterogeneous medium. Chin. J. Geophys. 49, 913–921.

Liu, Q.Y., Kind, R., Li, S.C., 1996. Maximal likelihood estimation and nonlinear inversion of the complex receiver function spectrum ratio. Chin. J. Geophys. 39, 500–511 (in Chinese with English Abstract).

Makeyeva, L.I., Vinnik, L.P., Roecker, S.W., 1992. Shear-wave splitting and small-scale convection in the continental upper mantle. Nature 358, 144–146.

Meissner, R., Mooney, W.D., Artemieva, I., 2002. Seismic anisotropy and mantle creep in young orogens. Geophys. J. Int. 149, 1–14.

Mitrovica, J.X., Forte, A.M., 2004. A new inference of mantle viscosity based upon joint inversion of convection and glacial isostatic adjustment data. Earth Planet. Sci. Lett. 225, 177–189.

Moresi, L., Gurnis, M., 1996. Constraints on the lateral strength of slabs from three-dimensional dynamic flow models. Earth Planet. Sci. Lett. 138, 15–28.

Moresi, L., Dufour, F., Muhlhaus, H.B., 2003. A Lagrangian integration point finite element method for large deformation modeling of viscoelastic geomaterials. J. Comput. Phys. 184, 476–497.

Molnar, P., Tapponnier, P., 1975. Cenozoic tectonics of Asia: effects of a continental collision. Science 189, 419–425.

Niu, Z.J., Wang, M., Sun, H.R., Sun, J.Z., You, X.Z., Gan, W.J., Xue, G.J., Hao, J.X., Xin, S.H., Wang, Y.Q., Wang, Y.X., Li, B., 2005. Contemporary velocity field of crustal movement of Chinese mainland from Global Positioning System measurements. Chin. Sci. Bull. 50 (9), 939–941.

Peng, S.S., 1993. On the neotectonic movement in Tian Shan that reflected by the geodesic deformation survey. Intra-continental Earthquake 7, 136–141 (in Chinese with English Abstract).

Poupinet, G., Avouac, J.P., Jiang, M., Wei, S., Kissling, E., Herquel, G., Guilbert, J., Paul, A., Wittlinger, G., Su, H., Thomas, J.C., 2002. Intracontinental subduction and Palaeozoic inheritance of the lithosphere suggested by a teleseismic experiment across the Chinese Tien Shan. Terra Nova 14, 18–24.

Roecker, S.W., Sabitova, T.M., Vinnik, L.P., Burmakov, Y.A., Golvanov, M.I., Mamatkanova, R., Munirova, L., 1993. Three-dimensional elastic wave velocity structure of the western and central Tien Shan. J. Geophys. Res. 98, 15779–15795.

Schott, B., Schmeling, H., 1998. Delamination and detachment of a lithospheric root. Tectonophysics 296, 225–247.

Schubert, G., Turcott, D.L., Olsen, P., 2001. Mantle Convection in the Earth and Planets. Cambridge University Press, Oxford.

Stuwe, K., 2002. Geodynamics of the Lithosphere. Springer, Berlin.

Tackley, P.J., King, S.D., 2003. Testing the tracer ratio method for modeling active compositional fields in mantle convection simulations. Geochem. Geophys. Geosyst. 4, 8302, doi:10.1029/2001GC000214.

Travis, B.J., Anderson, C., Baumgardner, J., Gable, C.W., Hager, B.H., O'Connell, R.J., Olson, P., Raefsky, A., Schubert, G., 1990. A benchmark comparison of numerical methods for infinite Prandtl number thermal convection in two-dimensional Cartesian geometry. Geophys. Astrophys. Fluid Dyn. 55, 137–160.

Turcotte, D.L., Schubert, G., 1982. Geodynamics: Applications of Continuum Physics to Geological Problems. John Wiley & Sons, New York.

Vinnik, L.P., Saipekova, A.M., 1984. Structure of the lithosphere and asthenosphere of the Tien Shan. Ann. Geophys. 2, 621–626.

Vinnik, L.P., Roecker, S.W., Kosarev, G.L., Oreshin, S.I., Koulakov, I.J., 2002. Crustal structure and dynamics of the Tien Shan. Geophys. Res. Lett. 29, 2047, doi:10.1029/2002GL015531.

Wolfe, C.J., Vemon, F.L., 1998. Shear-wave splitting at central Tien Shan: evidence for rapid variation of anisotropic patterns. Geophys. Res. Lett. 25, 1217–1220.

Wang, Q., Ding, G.Y., Qiao, X.J., Wang, X.Q., You, X.Z., 2000. Recent rapid shortening of crust across the Tian Shan Mountains and relative motion of tectonic blocks in the north and south. Chin. Sci. Bull. 45, 1995–1999.

Weinberg, R.F., Schmeling, H., 1992. Polydiapirs: multi-wavelength gravity structure. J. Struct. Geol. 14, 425–436.

Xu, Y., Liu, F.T., Liu, J.H., Sun, R.M., He, J.K., 2000. Seismic tomography beneath northwestern orogenic belts and adjacent basins in Chinese continent. Sci. China (Ser. D) 30, 113–122 (in Chinese).

Xiao, X.C., Liu, X., Gao, R., 2004. The Crustal Structure and Tectonic Evolution of Southern Xinjiang, China. Commercial Publication House, Beijing (in Chinese with English abstract).

Zhao, D.P., Hasegawa, A., Horiuchi, S., 1992. Tomographic imaging of P and S wave velocity structure beneath Northeastern Japan. J. Geophys. Res. 97, 19909–19928.

Zhao, D.P., Hasegawa, A., Kanamori, H., 1994. Deep structure of Japan subduction zone as derived from local, regional, and teleseismic events. J. Geophys. Res. 99, 22313–22329.

Zhao, J.M., Liu, G.D., Lu, Z.X., Zhang, X.K., Zhao, G.Z., 2003. Lithospheric structure and dynamic processes of the Tianshan orogenic belt and the Junggar basin. Tectonophysics 376, 199–239.

Zhong, S.J., Zuber, M.T., Moresi, L.N., Gurnis, M., 2000. Role of temperature dependent viscosity and surface plates in spherical shell models of mantle convection. J. Geophys. Res. 105, 11063–11082.